University of Groningen

Milky Way archaeology and the dynamical signatures of mergers

Gomez, Facundo Ariel

IMPORTANT NOTE: You are advised to consult the publisher's version (publisher's PDF) if you wish to cite from it. Please check the document version below.

Document Version
Publisher's PDF, also known as Version of record

Publication date:
2010

[Link to publication in University of Groningen/UMCG research database](#)

Citation for published version (APA):
Gomez, F. A. (2010). *Milky Way archaeology and the dynamical signatures of mergers*. s.n.

Chapter 2

The short-term evolution of initially nearby orbits

Abstract[*]

We study the initial behaviour of nearby trajectories in the phase-space of integrable potentials. We perform a suite of frozen N-body simulations of Plummer spheres and develop a simple analytical model to describe the behaviour of orbits on short timescales. We show that nearby orbits may at first diverge very fast while at late times they do so linearly with time. The initial transient behaviour is commonly present in N-body systems, and has been attributed in the past to short-term (microscopic) N-body chaos driven by close encounters. However our analytic model shows that another interpretation is possible. We find that the initial divergence depends on the rapid changes of the coordinates and momenta along an orbit when projected onto the time-domain. We explicitly demonstrate this for the isochrone potential, in which case the separation of nearby orbits grows in proportion to $\sqrt{t}$ for $t \to 0$, explaining the steepness of the initial rate of divergence. Our results support previous suspicions that this phenomenon is transient and not necessarily related to an instability in the sense of non-integrable behaviour in the early stages of the dynamics of N-body systems.

Key words: stellar dynamics – methods: analytical – methods: N-body simulations – galaxies: kinematics and dynamics

---

2.1 Introduction

The problem of how exactly galaxies reach their final equilibrium configuration is still open. It is clear that in contrast to gases, two-body collisions between stars in galaxies are unlikely to be the driving mechanism to reach a relaxed state, since the associated timescales are exceedingly large (Binney & Tremaine, 2008). In an attempt to explain the road to equilibrium from a statistical mechanics point of view, Lynden-Bell (1967) introduced the concept of "violent relaxation". In this context, the relaxation is reached through the effects of a "violently changing" gravitational field. The detailed mechanics of this process remain to be understood (Arad & Lynden-Bell, 2005; Valluri et al., 2007; Vass et al., 2009).

Besides the statistical mechanics approach, it is also possible to study the problem of "relaxation" at the orbital level. It is then useful to introduce the concept of mixing, by which we mean how quickly nearby particle trajectories diverge in (phase) space as a function of time. In the case of time-independent gravitational potentials it is customary to classify mixing into two types. If the particles move in an integrable potential, their orbits will diverge in space as a power-law in time, e.g. Helmi & White (1999); Vogelsberger et al. (2008). This process is known as phase-mixing (Binney & Tremaine, 2008). However, when the potential admits a certain amount of chaos, there exist regions of phase-space where nearby orbits diverge exponentially, evidencing an extreme sensitivity to small changes in the initial conditions (Lichtenberg & Lieberman, 1983). This is known as chaotic-mixing (Kandrup, 1998; Kandrup & Sideris, 2003).

Since the 1970s N-body simulations have become the standard tool for studies of the dynamics of structures in the Universe. One of the first to focus on how N-body systems evolve was Miller (1964), who simulated a self-consistent system in virial equilibrium of 8 up to 32 particles distributed randomly in a cubic volume. Miller found that the trajectories of neighbouring particles diverged exponentially right from the start, a process now known as "Miller's instability".

The initial transient originally identified by Miller (1964) has been confirmed using numerical experiments with a significantly larger number of particles (Lecar, 1968; Kandrup & Mahon, 1994; Valluri & Merritt, 2000; Hemsendorf & Merritt, 2002; Valluri et al., 2007), as well as with various degrees of numerical softening (Kandrup & Sideris, 2001) both for integrable and chaotic potentials. Furthermore, there is evidence that the rate of divergence associated to this phase increases in proportion to the number of particles used (Goodman, Heggie & Hut, 1993; Hemsendorf & Merritt, 2002). However, because this instability only lasts for a very short timescale it has been argued that it does not necessarily imply that the system is (macroscopically) chaotic (Valluri & Merritt, 2000; El-Zant, 2002).

Given the discrete nature of N-body simulations, it is not surprising that chaoticity should be present in these systems. This is why efforts have been made to establish the extent up to which an N-body simulation may be considered a faithful representation of a dynamical system (e.g. Diemand et al., 2004; Binney, 2004). General agreement now exists that when a system is represented by a sufficiently large number of particles, its behaviour tends to that expected from the collision-

less Boltzmann equation, at least in a statistical sense (Kandrup & Smith, 1991; Quinlan & Tremaine, 1992; El-Zant, 2002; Hayes, 2003; Sideris, 2004).

So, while the existence of a continuum limit in N-body systems appears to be more or less established for long timescales, on short timescales the initial transient behaviour is more difficult to understand. Goodman, Heggie & Hut (1993); Hut & Heggie (2001) presented a model to estimate the Lyapunov timescale in the absence of softening in a system of N-bodies of the same mass. They find that encounters between particles with impact parameter $p \sim R/\sqrt{N}$ occur sufficiently frequently (once per crossing time) to lead to the exponential growth of infinitesimal perturbations on a timescale proportional to the crossing time (here R denotes the size of the system and N the number of particles used to represent it). They estimate $\Delta r \sim \Delta r_0 \mathrm{e}^{t/t_{\mathrm{cr}}}$, which thus implies that in a crossing-time t_{cr} the separation between particles has increased by an e-fold, i.e. a factor ~ 2.7 (see also Binney & Tremaine, 2008).

In this paper, we revisit the problem of the initial divergence of nearby orbits. We first explore the behaviour in frozen N-body Plummer spheres and the dependence on the numerical parameters used (number of particles and softening) as in previous works. We then develop an analytic model that describes the initial behaviour of nearby orbits in the corresponding integrable smooth Plummer potential. Perhaps surprisingly, we find that, under certain initial conditions, nearby orbits in the smooth potential depict an extremely rapid divergence on timescales comparable to a crossing time just like in the N-body case.

The structure of this paper is the following. In Section 2.2 we introduce our N-body simulations and compute the rate of divergence of nearby orbits for different choices of the numerical parameters. In Section 2.3 we present our analytic model and in Section 2.4 we compare it to the behaviour found in the N-body simulations. Finally, Section 2.5 presents our conclusions.

2.2 The initial evolution in N-body frozen Plummer spheres

For simplicity, we study the behaviour of nearby orbits in an N-body realisation of the Plummer sphere, i.e. a fully integrable (spherical) system. The associated density and potential satisfy

$$\rho(r) = \frac{3M}{4\pi b^3} \left(1 + \frac{r^2}{b^2} \right)^{-5/2} \quad \text{and} \quad \phi(r) = -\frac{GM}{\sqrt{r^2 + b^2}}. \tag{2.1}$$

We choose units such that $G = M = b = 1$ and the internal energy of the system is $E = -3\pi/64$. We define the crossing time of the system $t_{\mathrm{cr}} = R/V$ where $R = -GM^2/2E$ and $V^2 = -2E/M$.

N-body simulations are often used to model the dynamical evolution of galaxies and galaxy systems, even though the number of particles that present day computers can handle is smaller, often by several orders of magnitude, than the number of

stars present in a galaxy. This implies that the particles do not represent individual stars, but should be considered as Monte Carlo realisations of the distribution function of a galaxy.

To represent a dynamical system with a limited number of particles such as our N-body realisations of the Plummer sphere, and to avoid spurious 2-body relaxation, the gravitational force between particles is generally softened. The softening parameter ϵ ensures that when two particles come very close together, they still will experience a finite acceleration. Several studies have looked at the optimal combination of numerical parameters for a given problem (e.g. Merritt, 1996; Dehnen, 2001; Springel, Yoshida & White, 2001). Athanassoula et al. (2000) in particular, discuss the optimal combination of softening and number of particles for the specific case of the Plummer sphere. In this work, the optimal softening is defined as that which minimises the integrated weighted difference between the true force field and the force computed in the N-body simulation. Therefore, the optimal softening is that which gives the best representation of the force for a given N, and was found to be $\epsilon_{opt} = 0.84N^{-0.25}$ by Athanassoula et al. (2000).

Here we adopt this same scaling, and moreover for a given experiment with N particles, we explore three possibilities for the softening. We take a slightly smaller value for the optimal softening, namely $\epsilon_{opt} = 0.66N^{-0.25}$ for all our experiments except for that with $N = 128,000$ for which we use $\epsilon_{opt} = 0.53N^{-0.25}$. We also consider two additional cases: $\epsilon' = 0.1\epsilon_{opt}$ and $\epsilon'' = 0.01\epsilon_{opt}$. In all our experiments, the numerical values of the softening ϵ_{opt} and ϵ' are smaller than the average inter-particle separation $R/N^{1/3}$, while ϵ' and ϵ'' are both smaller than the impact parameter of dominant encounters $R/\sqrt{N}$ as estimated by Goodman, Heggie & Hut (1993); Binney & Tremaine (2008). Therefore, we expect the effect of close encounters to be apparent in the rate of divergence of nearby orbits especially in these two latter cases.

We generate N-body realisations of the Plummer sphere with $N = 1,000$ up to $128,000$ particles in increasing powers of 2. As Kandrup & Sideris (2001) we follow the evolution of 100 nearby orbits in these frozen (in time and space) N-body systems. We use a Runge-Kutta-Fehlberg algorithm of order 4–5 for the orbital integration, with a variable timestep (the maximum tolerance is 10^{-8}). Our 100 orbits are distributed according to a multivariate Gaussian in phase-space with initial dispersion $\sigma_{x,0} = 10^{-5}$ and $\sigma_{v,0} = 10^{-3}$ around an orbit with pericentre 0.37, apocentre 1.64 and radial period 1.17 t_{cr}.

Figure 2.1 shows the evolution of the average separation $\langle\Delta_r\rangle$ of the ensemble of the above-mentioned 100 orbits for different values of N, where we have used the ϵ_{opt} value for the softening. This Figure shows that in all cases, an initial transient occurs, in which the orbits diverge very rapidly, increasing their separation by a factor $e^6 \sim 400$ on a timescale of one crossing time. Afterwards, the growth rate saturates and a new regime appears in which the growth is approximately linear in time. The separation reached after the initial transient is smaller than the impact parameter of dominant encounters for all N, and is roughly 1% of the scale of the system. It only becomes comparable to this impact parameters' scale after $5t_{\mathrm{cr}}$, but
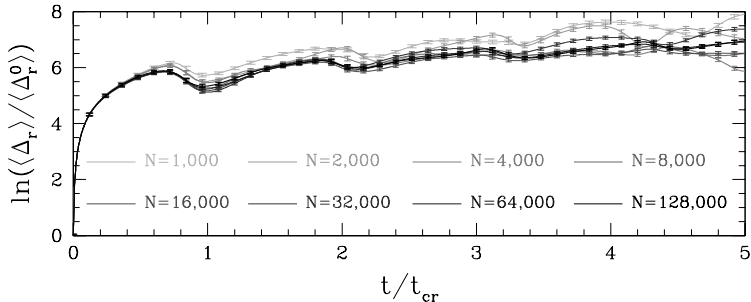
Figure 2.1: Evolution of the average separation of nearby orbits in frozen N-body simulations of a Plummer sphere with varying number of particles (from 1,000 up to 128,000). The force computations have used the optimal softening for each N (see text for details).

is still significantly smaller than the extent of the system.

Therefore, Figure 2.1 shows that over the timescales considered here, the behaviour is quite similar for all N, which testifies to the good choice of the softening proposed by Athanassoula et al. (2000).

In Figure 2.2 we explore the divergence in the frozen N-body simulations for different values of the softening. In all cases, we have used softenings which are smaller by a factor 10 (dark grey) and 100 (light grey) from the optimal values (in black). This Figure shows that a dependence of the rate of divergence on the softening exists, in the sense that the smaller ϵ the faster the divergence. However, this is only noticeable after 1-2 t_{cr} and even later for the larger N experiments. The amplitude of the initial transient ($t < t_{cr}$), which dominates the growth over the period considered in this Figure, does not depend on the particular value of N or ϵ.

These experiments suggest that the initial transient is a generic feature of the system, independent of the specific choice of numerical parameters. It occurs on a timescale comparable to a crossing time, but does not appear to be driven by single encounters, since systems with very small (or no) softening do not experience a stronger initial divergence.

Note as well, that the initial divergence has a much larger amplitude that estimated by the model of Goodman, Heggie & Hut (1993), suggesting that 2-body encounters of the type described in their work are not the driver of the initial very rapid divergence observed in our N-body systems. It is possible, nonetheless that this class of encounters are relevant at later times (between 1 and 5 t_{cr}, which is the point when the impact parameter is comparable to the separation) but only for the experiments with the smallest softenings.

The results of our experiments are in very good agreement with previous reports on the same problem. For example Kandrup & Sideris (2001) have run a similar set of experiments (their Figure 2) and found essentially the same initial growth as that shown in Figure 1. Valluri & Merritt (2000) also find for their triaxial ellipsoid
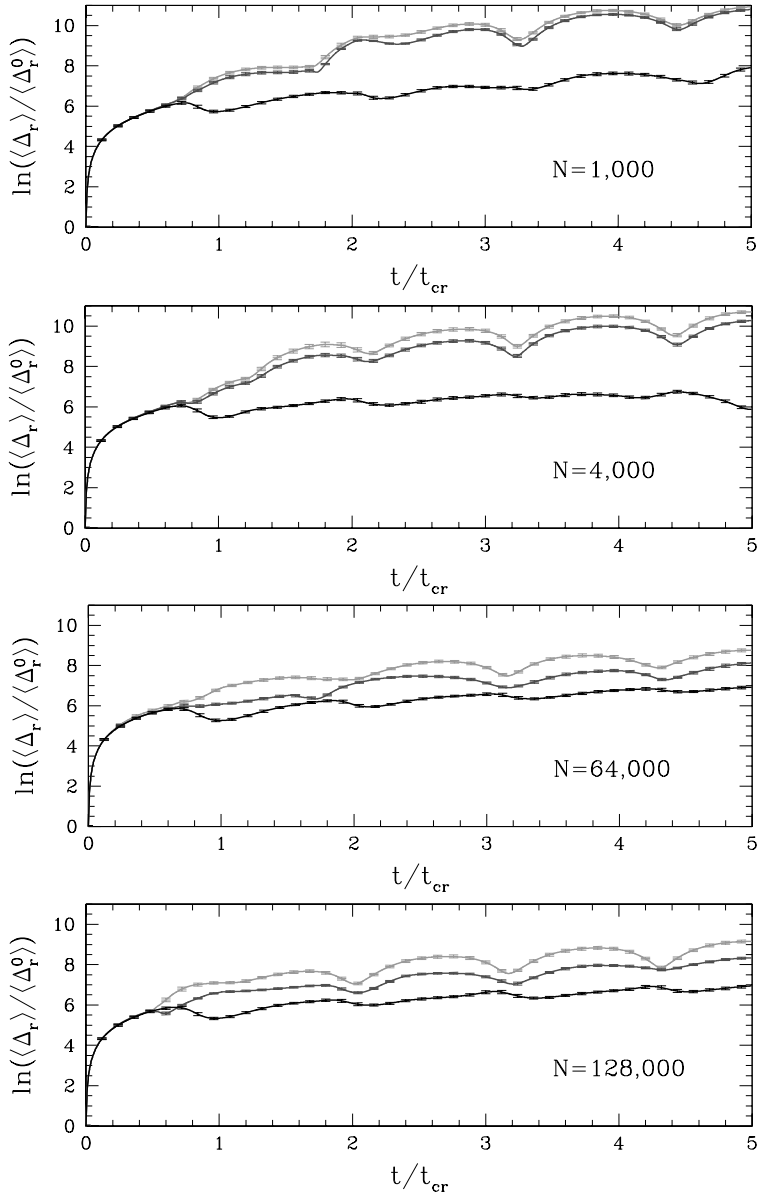
Figure 2.2: Evolution of the average separation of nearby orbits in N-body simulations of a Plummer sphere using different numbers of particles N and softening values for the force. The black curves correspond to ϵ_{opt} while dark and light grey to 10% and 1% of ϵ_{opt} respectively.

experiments that the divergence is initially very fast, after which and for large N, it saturates when it is of order 1% of the system size. Our experiments are also consistent with the results of Hemsendorf & Merritt (2002) on a timescale comparable to a crossing time. However we do not find the reported very large increase by factors e^{120} for longer timescales (up to 7 crossing times). There are three possible causes for the difference: i) the effect of round-off errors, which will be larger in their case because of the initial orbit separation 10^{-30}, well below the value we have considered and what is possible to follow with double precision; ii) they integrate the "variational equations" without softening; iii) our systems, unlike theirs, are frozen N-body experiments, which implies that we are probably underestimating the effect of the propagation of "errors" triggered by encounters.

2.3 Analytic description of the evolution in phase-space of nearby orbits

Helmi & White (1999) developed a formalism to follow the evolution in time and in phase-space of a distribution function representing an initial cluster of particles orbiting an external gravitational field.

The basic idea behind their approach consists mapping the initial system (a cluster of stars or a satellite galaxy) onto action-angle space, then follow the much simpler evolution in this space, and finally transform back *locally* onto observable coordinates (all these being linear transformations; for a sketch see Figure 2.3). This method, which uses action-angle variables, is very general and can be applied to any potential that admits regular orbits (Goldstein, 1959; Binney & Tremaine, 2008). If the potential is separable such as in the case of the Plummer sphere, the implementation is simpler while still being generic.

2.3.1 The distribution function

Therefore, instead of following the evolution of pairs of nearby orbits as we have done in Section 2.2, we here follow the evolution of a distribution function in phase-space. In particular, and for simplicity, we assume that the initial distribution function of the system is a multivariate Gaussian in $\varpi = (\mathbf{x}, \mathbf{v})$ coordinates centred on $\langle \varpi_0 \rangle$ (a given particle or orbit):

$$f(\varpi, t_0) = f_0 \exp\left[-\frac{1}{2} \mathbf{\Delta}_{\varpi,0}^{\dagger} \sigma_{\varpi,0} \mathbf{\Delta}_{\varpi,0} \right] \tag{2.2}$$

where $\mathbf{\Delta}_{\varpi,0} = \varpi - \langle \varpi_0 \rangle$, and $\sigma_{\varpi,0}$ is the variance matrix (the inverse of the covariance matrix) at the initial time:

$$\sigma_{\varpi,0} = \left[\begin{array}{cc} \mathbf{S_{x,0}} & \mathbf{C_{xv,0}} \\ \mathbf{C_{xv,0}} & \sigma_{\mathbf{v,0}} \end{array} \right]. \tag{2.3}$$

For example, if the variance matrix is diagonal, then $\mathbf{S_x} = [1/\sigma_{x_i}^2 \delta_{ij}]$ and $\sigma_{\mathbf{v}} = [1/\sigma_{v_i}^2 \delta_{ij}]$, and $\mathbf{C_{xv}} = \mathbf{0}$.
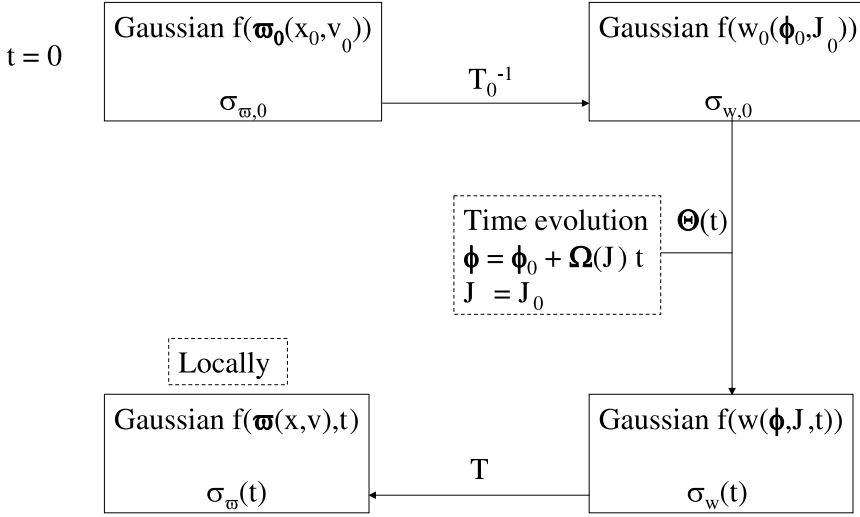
Figure 2.3: Flow chart showing the basic steps of our analytic formalism to measure the evolution of a system in phase-space.

To transform from configuration and velocity space to action-angle space we will use a mapping $\mathbf{T} : \varpi \to w = (\phi, \mathbf{J})$. This mapping will be linear provided the extent of the system in phase-space is small. Its elements are $T_{ij} = \partial \varpi_i / \partial w_j$ evaluated at $\langle \varpi \rangle$. Such a mapping will preserve the form of the distribution function, which will now be a Gaussian in action-angle space, with variance matrix $\sigma_{w,0} = \mathbf{T}_0^\dagger \sigma_{\varpi,0} \mathbf{T}_0$.

The dynamical evolution of the system in action-angle coordinates is given by $\phi = \phi_0 + \mathbf{\Omega}(\mathbf{J})\, t$, and $\mathbf{J} = cst$. Since we may express

$$\mathbf{\Delta}_w = \mathbf{\Theta}(t)\mathbf{\Delta}_{w,0} \qquad \text{with} \qquad \mathbf{\Theta}(t) = \begin{bmatrix} \mathcal{I}_3 & -\mathbf{\Omega}'t \\ \mathbf{0} & \mathcal{I}_3 \end{bmatrix},$$

where $\mathcal{I}_3$ is the identity matrix in 3-D, and $\mathbf{\Omega}'$ represents a 3×3 matrix whose elements are $\partial \Omega_i / \partial J_j$, the distribution function at time t becomes

$$f(\mathbf{w}, t) = f_0 \exp\left[-\frac{1}{2}\mathbf{\Delta}_w{}^\dagger \sigma_w \mathbf{\Delta}_w \right], \text{ with } \sigma_w = \mathbf{\Theta}(t)^\dagger \sigma_{w,0} \mathbf{\Theta}(t). \tag{2.4}$$

From this last Equation we may finally derive the distribution function in configuration and velocity space at time t. To this end, we perform a local transformation using the matrix $\mathbf{T}$. Since this is done locally, our distribution function is still a multivariate Gaussian. The variance matrix at time t is

$$\sigma_\varpi(t) = (\mathbf{T}_0\mathbf{\Theta}(t)\mathbf{T}^{-1})^\dagger \sigma_{\varpi,0}(\mathbf{T}_0\mathbf{\Theta}(t)\mathbf{T}^{-1}). \tag{2.5}$$

This variance matrix contains all the information about the dynamical properties of the particles on initially nearby orbits. For example, the evolution of the velocity
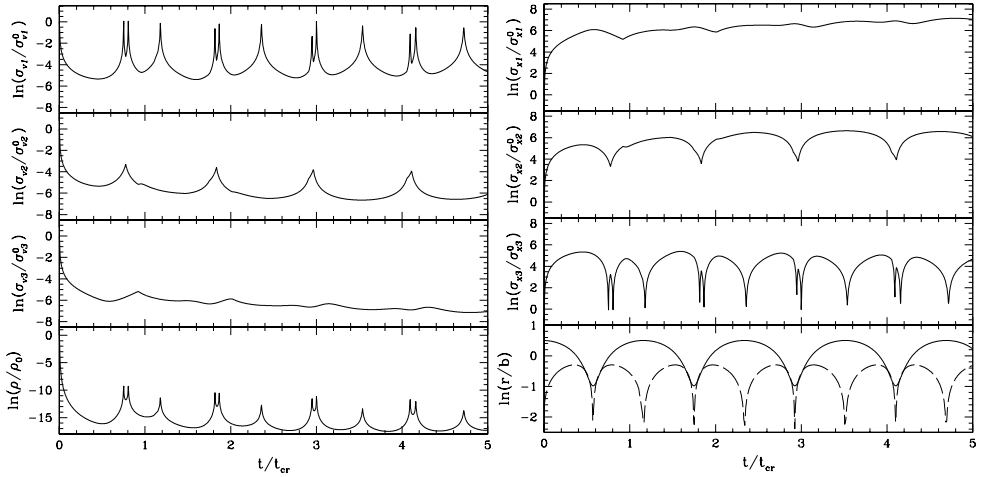
Figure 2.4: Time evolution of the velocity dispersions (top three panels on the left), spatial density (bottom left panel) and dispersions in configuration space (top three panels on the right), for a system moving in a Plummer potential on the orbit explored in Sec.2.2. The periodicity observed is related to the radial (and angular) orbital oscillations, as shown in the bottom panel on the right, where we have plotted the logarithm of $r(t)$ (solid) and $\sqrt{rp_r}(t)$ (dashed).

ellipsoid may be derived from the velocity submatrix: $\sigma_\mathbf{v}$. This submatrix describes the velocity distribution of nearby particles at time t. The spatial density at a particular location $\mathbf{x}$ at time t (which is related to the spatial separation of those particles) is obtained by integrating the distribution function with respect to all velocities:

$$\rho(\mathbf{x}, t) = (2\pi)^3 f_0 \sigma_{v_1} \sigma_{v_2} \sigma_{v_3} \times \exp\left[-\frac{1}{2}\boldsymbol{\Delta}_x{}^\dagger \sigma_\mathbf{x} \boldsymbol{\Delta}_x\right] \tag{2.6}$$

where $\sigma_{v_{i=1,2,3}}$ are the velocity dispersions along the principal components of the velocity ellipsoid. The matrix $\sigma_\mathbf{x}$ is 3×3, and contains all the information concerning the evolution of the particle distribution in configuration space, including their separation, which is ultimately, the quantity that we want to measure.

2.3.2 Application to the Plummer potential

As in Section 2.2 we assume that the initial variance matrix of the particle distribution $\sigma_{\varpi,0}$ is diagonal (see Eq. 2.3), with $\mathbf{S_{x,0}} = [1/\sigma_{x,0}^2 \delta_{ij}]$ and $\sigma_{\mathbf{v},0} = [1/\sigma_{v,0}^2 \delta_{ij}]$, and where $\sigma_{x,0} = 10^{-5}$ and $\sigma_{v,0} = 10^{-3}$. We centre this distribution on the orbit used in the N-body simulations of Sec. 2.2.

In Figure 2.4 we plot the evolution of the velocity dispersions, the spatial density and the dispersions in configuration space. These quantities have been computed using the procedure outlined above. This Figure shows that in the case of spherical potentials, only two of the velocity dispersions decrease in time, while the third one

remains on average constant (it corresponds to the direction perpendicular to the plane of motion). These results imply that the configuration-space dispersions will increase in time, as a consequence of Liouville's theorem (i.e. the conservation of phase-space density). This can also be seen from $dM \sim \rho \times \sigma_{x_1}\sigma_{x_2}\sigma_{x_3} = cst.$

The explicit form of the dispersions in velocity and in configuration space has been derived in the Appendix. There we work in a reference frame that coincides with the plane of motion (this is of course possible for a spherical potential). In this new frame only two coordinates and two velocities are required to specify completely the state of system. In this case, the spatial density

$$\rho \propto \sigma_{v_1}\sigma_{v_2} = (\lambda_{v_1}\lambda_{v_2})^{-1/2}, \tag{2.7}$$

where λ_v denotes the eigenvalues of the velocity submatrix $\sigma_{\mathbf{v}}$, and for which the following relation holds

$$\lambda_{v_1}\lambda_{v_2} = \frac{r^2 p_r^2}{\Omega_r^2}\left(\alpha_4 t^4 + \alpha_3 t^3 + \alpha_2 t^2 + \alpha_1 t + \alpha_0\right). \tag{2.8}$$

The coefficients α_i depend both on location along the orbit as well as on the initial extent of the system in phase-space (see Eq. 2.18). The decrease in the spatial density of the system observed in Fig. 2.4 can thus be understood from Eqs. (2.7) and (2.8). The strong enhancements in the density seen in Fig. 2.4 take place at the orbital turning points: when $p_r = 0$ then $\lambda_{v_1} \times \lambda_{v_2} \to 0$ and hence $\rho \to \infty$.

In the Appendix we show that the configuration-space dispersions satisfy $\sigma_{x_1}\sigma_{x_2} = \sqrt{\frac{\lambda_{v_1}\lambda_{v_2}}{\det \sigma_w^0}}$ (see Eq. 2.24). Close inspection of Eqs. (2.8) and (2.18), allows us to reach the following conclusions:

- For very short timescales, the term with α_0 dominates. In this case the separation of nearby orbits as measured by σ_{x_i} purely reflects the rapid changes in the coordinates and momenta along the orbit when projected onto the time-domain (i.e. this term is heavily weighted by $r^2 p_r^2$).

- The terms with α_2 and α_4 are always positive, implying that these will induce a rapid increase in the λ_v, and hence of the dispersions in configuration space on intermediate timescales.

- The terms with α_1 and α_3 can either be positive or negative, depending on location along the orbit. This (partly) explains the strong oscillatory behaviour observed in Fig. 2.4.

- On longer timescales, only the term with $\alpha_4 t^4$ is important. This gives rise to the secular behaviour of density which decreases as $1/t^2$ (as found by Helmi & White, 1999), and for the dispersions in configuration-space to increase in linear proportion to t.

The behaviour just described applies to orbits in any spherical potential. In general the exact time-variation of the various coefficients in Eq. (2.8) is rather complex. However, in the case of the isochrone potential, it is possible to find the

relation between the action-angle variables and the coordinates in configuration and velocity space exactly (Binney & Tremaine, 2008). This allows the derivation of the explicit functional form of each of the terms in Eq. (2.8).

Particularly relevant in the context of this Paper, is the behaviour of the term $\alpha_0 \times r^2 p_r^2$ since this will set the short-term (rate of) divergence of nearby orbits. For the isochrone potential

$$r^2 p_r^2 = C \sin^2 \Psi, \tag{2.9}$$

where C is a constant dependent on the energy and angular momentum of the orbit and on the scale and mass of the system (McGill & Binney, 1990; Gerhard & Saha, 1991). Ψ is related to the radial angle ϕ_r

$$\phi_r = \phi_{0,r} + \Omega_r t = \Psi - C' \sin \Psi. \tag{2.10}$$

In the case of the Kepler potential (which is a limiting case of the isochrone potential), Ψ is the mean anomaly. Note that for small t, and assuming $\phi_{0,r} = 0$ (i.e. the integration starts at a radial turning point) then $\Psi \propto t$. If we further assume that α_0 is constant (a condition satisfied if $\sigma_{x,0} \ll \sigma_{v,0}$) then

$$\lambda_{v_1} \lambda_{v_2} \propto r^2 p_r^2 \propto \sin^2 \Psi \propto t^2. \tag{2.11}$$

This implies for example that the density will initially decrease as $\rho \propto 1/t$, i.e. its rate of decline diverges as $t \to 0$. Even though we have derived this dependence explicitly only for the isochrone potential, we expect this result to be valid more generally. The bottom left panel of Figure 2.4, which depicts the evolution of the density for the Plummer potential shows that this indeed appears to be the case.

2.3.3 Separation in configuration space and dependence on initial conditions

To establish the relation between the dispersions in configuration space (i.e. the inverse of the eigenvalues of the matrix $\sigma_{\mathbf{x}}$) and the separation between nearby orbits we proceed as follows.

We integrate 1,000 orbits with initial conditions following the same 6D Gaussian used in the previous section (i.e configuration space dispersion $\sigma_{x,0} = 10^{-5}$ and velocity dispersion $\sigma_{v,0} = 10^{-3}$ centred also around the same orbit). We then measure the separation $\Delta_{r,i}^{\mathrm{smooth}} = |\mathbf{r}_i - \mathbf{r_0}|$ between this orbit and the 1,000 neighbouring trajectories, and derive the average $\langle \Delta_r^{\mathrm{smooth}} \rangle$. We compare this separation to three different averages of the configuration-space dispersions obtained from our analytic model:

1. the geometric mean: $\Delta_g = (\sigma_{x_1} \sigma_{x_2} \sigma_{x_3})^{1/3}$,

2. the arithmetic mean: $\Delta_a = (\sigma_{x_1} + \sigma_{x_2} + \sigma_{x_3})/3$,

3. the modulus: $\Delta_m = \sqrt{\sigma_{x_1}^2 + \sigma_{x_2}^2 + \sigma_{x_3}^2}/3$.
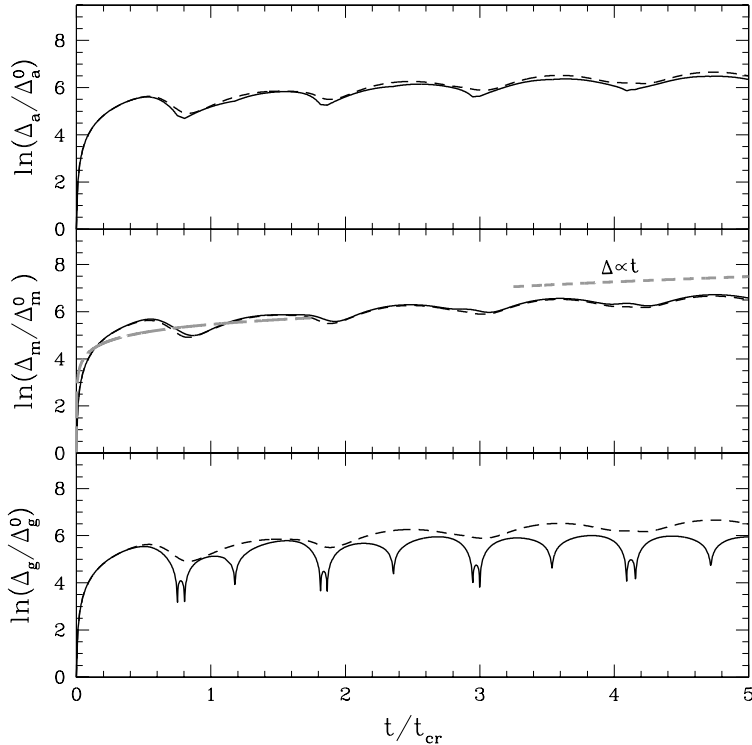
Figure 2.5: Time evolution of three possible averages of the dispersions in configuration-space obtained through our formalism. The black dashed curve in each panel represents the average separation $\langle\Delta_r\rangle$ of 1,000 nearby orbits. Note the excellent agreement between $\langle\Delta_r\rangle$ and Δ_m as shown in the middle panel. In this panel, the grey long-dashed curve is proportional to $\sqrt{t}$ and follows well the very steep initial growth of $\langle\Delta_r\rangle$. On the other hand, at late times the separations increase linearly as shown by the short-dashed grey curve.

The various panels in Figure 2.5 show the behaviour of these means compared to the average obtained directly from the integrations of the 1,000 nearby trajectories (dashed curve). As can be seen from this Figure the three averages perform equally well for short timescales. On the other hand, for longer timescales it is the modulus Δ_m of the configuration-space dispersions which provides the best match to the separation between nearby orbits $\langle\Delta_r^{\mathrm{smooth}}\rangle$.

Figure 2.5 shows that the separation of nearby orbits in smooth integrable potentials exhibits a rapid initial divergence, which is followed by a secular increase which is linear in time. The initial transient occurs in a completely integrable system. It reflects the way the phase-space curves around an orbit with time, as shown in the Appendix. In the case of the isochrone potential, the explicit time-dependence of the initial transient can be derived analytically. As discussed above,
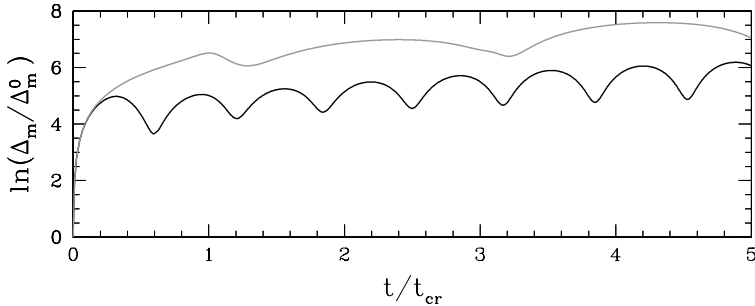
Figure 2.6: Time evolution of the separation of nearby orbits as measured by Δ_m for two different orbits: the black curve is for an inner orbit, while grey corresponds to an orbit with a large apocentre.

$\Delta_g \propto \sqrt{\sigma_{x_1} \times \sigma_{x_2}} \propto (\lambda_{v_1} \lambda_{v_2})^{1/4} \propto \sqrt{t}$ from Eq. (2.11). This shows that the separation of nearby orbits as measured by the geometric mean Δ_g has a very steep rate of increase with time, since $d\Delta_g/dt \propto 1/\sqrt{t} \to \infty$ as $t \to 0$. The grey curve in the middle panel of Figure 2.5 shows that this functional form describes well the behaviour also in the case of an orbit in a Plummer sphere.

Thus far we have only explored one initial configuration for the orbit and for the variance matrix. We now focus on how the separation of nearby orbits depends on their location in phase-space. The black curve in Figure 2.6 shows Δ_m for an orbit constrained to move in the inner regions of the system (pericentre $r_p = 0.12$ and apocentre $r_a = 0.84$), while the grey curve has a much larger apocentre $r_a = 2.87$ ($r_p = 0.21$). Clearly the amplitude of the initial transient depends on the regions of phase-space the orbits probe. We also find a slight dependence on the initial location along the orbit, namely that the initial divergence has the largest amplitude (and it lasts longer) when the integration is started near an orbital turning point.

However, the largest influence on the initial rate of divergence comes from the form of the initial variance matrix. The examples discussed thus far consider $\sigma_{x,0} = 10^{-5}$ and $\sigma_{v,0} = 10^{-3}$. We have found that by decreasing $\sigma_{x,0}/\sigma_{v,0}$, the amplitude of the divergence can be made exceedingly large. However, as we will show below it can also be made negligibly small if $\sigma_{x,0} \gg \sigma_{v,0}$.

2.4 Comparison to N-body simulations

The behaviour visible in Figure 2.5 is strikingly similar to that observed in the N-body simulations discussed in Sec. 2.2. This is explicitly demonstrated in the top panel of Fig. 2.7, where we compare our analytic estimates (Δ_m, dashed) to the average separation of 100 orbits integrated in the N-body representation of the system ($\langle \Delta_r \rangle$, solid curve), with $N = 128k$ for the optimal softening case and for $\sigma_{v,0} \gg \sigma_{x,0}$.

This Figure suggests that the initial divergence previously reported to be present
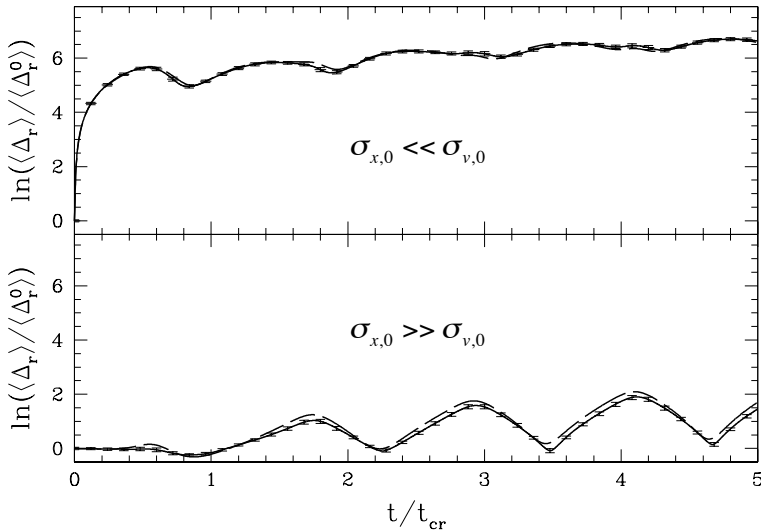
Figure 2.7: Time evolution of the average separation $\langle \Delta_r \rangle$ of 100 nearby orbits integrated in a frozen N-body realisation of the Plummer sphere with $N = 128,000$ and ϵ_{opt} (solid curve). The error bars denote the error on this average. The dashed curve represents the separation of nearby orbits as measured by Δ_m using our analytic prescription. The different panels show the dependence of the rate of divergence on the initial configuration of the set of nearby orbits, where top (bottom) corresponds to more (less) strongly clustered in configuration than in velocity space.

in N-body simulations, and shown in Figures 2 and 3 of this paper, is intrinsic to gravitational systems. As shown in Section 2.3.2, it results from the distortion of the phase-space neighbourhood of an orbit when studied in the time domain. The rate of divergence is very large as it evolves as $1/\sqrt{t}$ near $t \to 0$.

The near saturation of the rate of divergence after roughly one orbital period, indicates that this transient behaviour cannot be related to dynamical chaos. For example, for a chaotic orbit in a non-integrable potential this saturation is never reached as shown by Vogelsberger et al. (2008) (see their Fig. 6).

The bottom panel of Figure 2.7 shows that the initial transient may disappear completely both in the analytic model as in the N-body simulations when the initial system is more strongly clustered in velocity than in configuration space. Here we have used $\sigma_{v,0} = 10^{-5}$ and $\sigma_{x,0} = 10^{-3}$. We have noticed that the orbital integrations in the N-body experiments reported in the literature often start from a configuration such as that depicted in the top panel. In such cases, nearby orbits are drawn within a specific (small) region of configuration space, but are free to have any range of initial velocities (e.g. Kandrup & Sideris, 2001).

In light of the discussion above, we may reach the following conclusions. In N-body systems with the appropriate (optimal) value of the softening, the initial rate

of divergence is reproduced very well by our model, and has a "geometric" origin. However, in N-body simulations with a very small or no softening, such as those discussed by Goodman, Heggie & Hut (1993); Hut & Heggie (2001) and Valluri & Merritt (2000) we expect a steep initial divergence as in our model *only* for orbits initially (much) more strongly clustered in space than in velocity. Under a different initial configuration, nearby orbits may diverge due to 2-body encounters but this divergence should typically have a lower amplitude. For all initial configurations, and after a crossing time, such encounters are likely important in driving the evolution of the separation of nearby orbits.

2.5   Discussion and Conclusions

We have studied the initial divergence of nearby orbits in frozen N-body simulations of a Plummer sphere, and have explored the dependencies of this divergence on numerical parameters, in particular softening and number of particles. In very good agreement with previous work, we have found that the rate of divergence is initially very fast, and that roughly after one crossing time, it saturates. At this point in time the separation is much smaller than the scale of the system.

   We then developed an analytic model to follow the separation of nearby orbits in a smooth Plummer potential. This model shows that nearby orbits will diverge very fast initially even for fully integrable smooth potentials, provided they are strongly clustered in space and less in velocity. This divergence is driven by the time-evolution of the distortion of the phase-space around an orbit and is a generic feature of dynamical systems. We have been able to show explicitly that nearby orbits in the isochrone potential diverge initially in proportion to $\sqrt{t}$, i.e. as $t \to 0$ the rate of separation effectively diverges.

   Therefore, the initial extremely rapid divergence of nearby orbits previously reported in N-body systems does not inevitably imply a manifestation of microscopic chaos on a crossing timescale. This transient phenomenon is not necessarily related to an instability in the sense of non-integrable behaviour in the short-term dynamics of N-body systems.

Acknowledgements

Appendix 2.A   Matrices in a spherical potential

For spherical potentials $\Phi(r)$, we may choose a system of coordinates that coincides with the plane of motion of the system. In this plane the position of a particle is specified by its angular (ψ) and radial (r) coordinates. The actions of an orbit in this case are:

$$L = J_\psi = p_\psi, \quad J_r = \frac{1}{\pi} \int_{r_1}^{r_2} dr \frac{1}{r} \sqrt{2[E - \Phi(r)]r^2 - L^2}, \tag{2.12}$$

where L is the total angular momentum of the particle, E is its energy, and r_1 and r_2 the orbital turning points.

In order to track the evolution of the dispersions of our initial distribution function, $f(\varpi, t_0)$, we perform the following sequence of operations. Firstly, we transform from Cartesian coordinates $\varpi = (\mathbf{x}, \mathbf{v})$ to action angle variables $w = (\theta, \mathbf{J})$. The distribution function is then evolved in this space, after which, we transform back to Cartesian coordinates (see Figure 2.3).

For the sake of simplicity, here we begin with a distribution function already expressed in terms of the action-angle variables and we also assume that, initially, the variance matrix is diagonal, i.e., $\sigma_{w,0} = [\sigma_{ii}\delta_{ij}]$. With the time evolution operator, $\boldsymbol{\Theta}(t)$, known, we can compute the variance matrix at any given time t as $\sigma_w(t) = \boldsymbol{\Theta}(t)^\dagger \sigma_{w,0} \boldsymbol{\Theta}(t)$. Equation (2.4) shows $\boldsymbol{\Theta}(t)$ for the 3-D case, but we reduce the equation for our purposes to the 2-D case.

After evolving the system in the action-angle space we need to transform back locally to configuration and momenta space $\hat{\omega} = (\mathbf{x}, \mathbf{p})$ using the transformation matrix $\mathbf{T}^{-1}$. The elements of this matrix are related to the second derivatives of the characteristic function $W(\mathbf{q}, \mathbf{J})$. In our case

$$\mathbf{T^{-1}} = \begin{bmatrix} 1 & t_{12} & t_{13} & t_{14} \\ 0 & t_{22} & t_{23} & t_{24} \\ 0 & 0 & 1 & 0 \\ 0 & t_{42} & t_{43} & t_{44} \end{bmatrix}, \tag{2.13}$$

with

$$t_{12} = -\frac{h(r)}{\Omega_r}W_{34} + \frac{\kappa}{p_r}, \quad t_{13} = W_{33} + W_{34}t_{43}, \quad t_{14} = W_{34}t_{44},$$
$$t_{22} = -\frac{h(r)}{\Omega_r}W_{44} + \frac{\Omega_r}{p_r}, \quad t_{23} = W_{34} + W_{44}t_{43}, \quad t_{24} = W_{44}t_{44},$$
$$t_{42} = -\frac{h(r)}{\Omega_r}, \qquad\qquad t_{43} = -\frac{\kappa}{\Omega_r}, \qquad\qquad t_{44} = \frac{p_r}{\Omega_r},$$

where

$$h(r) = -\Phi'(r) + \frac{L^2}{r^3}, \quad p_r = \sqrt{2[E - \Phi(r)] - \frac{L^2}{r^2}}, \quad \kappa = \Omega_\psi - \frac{L}{r^2},$$

and

$$W_{33} = \frac{\partial^2 W}{\partial L^2} = \int_{r_1}^{r} \frac{dr}{p_r} \left(\frac{\partial \Omega_\psi}{\partial J_\psi} - \frac{1}{r^2} - \frac{\kappa^2}{p_r^2} \right),$$

$$W_{44} = \frac{\partial^2 W}{\partial J_r^2} = \int_{r_1}^{r} \frac{dr}{p_r} \left(\frac{\partial \Omega_r}{\partial J_r} - \frac{\Omega_r^2}{p_r^2} \right),$$

$$W_{34} = \frac{\partial^2 W}{\partial L \partial J_r} = \int_{r_1}^{r} \frac{dr}{p_r} \left(\frac{\partial \Omega_\psi}{\partial J_r} - \frac{\kappa}{p_r^2} \Omega_r \right).$$

Subindices 1 and 3 in the expressions above refer to directions associated with ψ, such as, ϕ_ψ and J_ψ whereas 2 and 4 are related to r. For more details about this procedure we refer the reader to Helmi & White (1999).

Given $\mathbf{T}^{-1}$, the variance matrix at time t is expressed as:

$$\sigma_{\hat{\omega}}(t) = (\mathbf{\Theta}(t)\mathbf{T}^{-1})^\dagger \sigma_{w,0} (\mathbf{\Theta}(t)\mathbf{T}^{-1}). \tag{2.14}$$

where the elements t_{ij} are evaluated at $\langle \mathbf{x}(t) \rangle$. Substituting $\mathbf{T}^{-1}$, $\mathbf{\Theta}(t)$ and $\sigma_{w,0}$ in the above expression, then

$$\sigma_{\hat{\omega}}(t) = \begin{bmatrix} \sigma_{11} & \sigma_{11}A & \sigma_{11}B \\ \{1,2\} & \sigma_{11}A^2 + \sigma_{22}D^2 + \sigma_{44}t_{42}^2 & \sigma_{11}AB + \sigma_{22}DE + \sigma_{44}t_{42}t_{43} \\ \{1,3\} & \{2,3\} & \sigma_{11}B^2 + \sigma_{22}E^2 + \sigma_{33} + \sigma_{44}t_{43}^2 \\ \{1,4\} & \{2,4\} & \{3,4\} \end{bmatrix}$$

$$\left. \begin{array}{c} \sigma_{11}C \\ \sigma_{11}AC + \sigma_{22}DF + \sigma_{44}t_{42}t_{44} \\ \sigma_{11}BC + \sigma_{22}EF + \sigma_{44}t_{43}t_{44} \\ \sigma_{11}C^2 + \sigma_{22}F^2 + \sigma_{44}t_{44}^2 \end{array} \right], \tag{2.15}$$

where

$$A = t_{12} - \Omega'_{34}t_{42}t, \quad B = t_{13} - (\Omega'_{33} - \Omega'_{34}t_{43})t, \quad C = t_{14} - \Omega'_{34}t_{44}t,$$
$$D = t_{22} - \Omega'_{44}t_{42}t, \quad E = t_{23} - (\Omega'_{34} - \Omega'_{44}t_{43})t, \quad F = t_{24} - \Omega'_{44}t_{44}t.$$

In general, one is more interested in the properties of the debris in velocity space, rather than in momenta space. Therefore we transform the variance matrix according to $\sigma_\varpi(t) = \mathbf{T}^\dagger_{p \to v} \sigma_{\hat{\omega}}(t) \mathbf{T}_{p \to v}$, with

$$\mathbf{T}_{p \to v} = \begin{bmatrix} 1 & 0 & 0 & 0 \\ 0 & 1 & 0 & 0 \\ 0 & v_\psi & r & 0 \\ 0 & 0 & 0 & 1 \end{bmatrix}.$$

To obtain an expression for the time evolution of the velocity dispersions we focus our attention on what happens around a particular point $\langle \mathbf{x}(t) \rangle$ in configuration

space located on the mean orbit of the system. This is equivalent to studying the velocity submatrix of the variance matrix $\sigma_\varpi(t)$, that is

$$\sigma_{\mathbf{v}} = \begin{bmatrix} r^2(\sigma_{11}B^2 + \sigma_{22}E^2 + \sigma_{33} + \sigma_{44}t_{43}^2) & r(\sigma_{11}BC + \sigma_{22}EF + \sigma_{44}t_{43}) \\ \{1,2\} & \sigma_{11}C^2 + \sigma_{22}F^2 + \sigma_{44}t_{44}^2 \end{bmatrix}. \quad (2.16)$$

By diagonalising the matrix $\sigma_{\mathbf{v}}$ we obtain the principal axes of the velocity ellipsoid at the point $\langle \mathbf{x}(t) \rangle$, and the associated dispersions. The eigenvalues of $\sigma_{\mathbf{v}}$ are the roots of the characteristic equation: $\det[\sigma_{\mathbf{v}} - \lambda \mathcal{I}] = 0$. An interesting quantity is for example, $\lambda_{v_1}\lambda_{v_2}$ because it is inversely proportional to the density: $\rho \propto \sigma_{v_1}\sigma_{v_2} = (\lambda_{v_1}\lambda_{v_2})^{-1/2}$. In our case:

$$\lambda_{v_1}\lambda_{v_2} = \frac{r^2 p_r^2}{\Omega_r^2} \left(\alpha_4 t^4 + \alpha_3 t^3 + \alpha_2 t^2 + \alpha_1 t + \alpha_0 \right), \quad (2.17)$$

where

$$
\begin{aligned}
\alpha_4 &= \sigma_{11}\sigma_{22}(\det \mathbf{\Omega}')^2, \\
\alpha_3 &= 2\sigma_{11}\sigma_{22} \det \mathbf{\Omega}' \, (2W_{34}\Omega_{34}' - W_{33}\Omega_{44}' - W_{44}\Omega_{33}'), \\
\alpha_2 &= \sigma_{11}\sigma_{22}\big(2\det \mathbf{\Omega}' \det \mathbf{W} + (\Omega_{44}'W_{33} + \Omega_{33}'W_{44})^2 + \\
&\quad 4W_{34}(\Omega_{34}'^2 W_{34} - \Omega_{33}'\Omega_{34}'W_{44} - \Omega_{34}'\Omega_{44}'W_{33})\big) + \\
&\quad (\sigma_{11}\sigma_{33} + \sigma_{22}\sigma_{44})\,\Omega_{34}'^2 + \sigma_{11}\sigma_{44}\Omega_{33}'^2 + \sigma_{22}\sigma_{33}\Omega_{44}'^2, \\
\alpha_1 &= 2\big(\sigma_{11}\sigma_{22} \det \mathbf{W} \, (2\Omega_{34}'W_{34} - \Omega_{44}'W_{33} - \Omega_{33}'W_{44}) - \\
&\quad \Omega_{34}'W_{34} \, (\sigma_{11}\sigma_{33} + \sigma_{22}\sigma_{44}) - \sigma_{11}\sigma_{44}\Omega_{33}'W_{33} - \\
&\quad \sigma_{22}\sigma_{33}\Omega_{44}'W_{44}\big), \\
\alpha_0 &= (\sigma_{11}\sigma_{22})(\det \mathbf{W})^2 + W_{34}^2 \, (\sigma_{11}\sigma_{33} + \sigma_{22}\sigma_{44}) + \\
&\quad \sigma_{11}\sigma_{44}W_{33}^2 + \sigma_{22}\sigma_{33}W_{44}^2 + \sigma_{33}\sigma_{44}, \quad (2.18)
\end{aligned}
$$

with

$\det \mathbf{W} = W_{33}W_{44} - W_{34}^2.$

These equations explicitly show the behaviour of principal axes velocity dispersions:

- For very short timescales, the term with α_0 dominates. In this case the behaviour purely reflects the geometry of the orbit in phase space (being heavily weighted by $r^2 p_r^2$).

- The terms with α_2 and α_4 are always positive, implying that these will induce a rapid increase in the λ_v, or a rapid decrease of the velocity dispersions on intermediate timescales.

- The terms with α_1 and α_3 can either be positive or negative, depending on location along the orbit (i.e. the W_{ij} vary in magnitude and sign). This explains the strong oscillatory behaviour observed in Fig. 2.4.

- On longer timescales, only the term $\alpha_4 t^4$ is important. This gives rise to the secular behaviour of density which decreases as $1/t^2$, and the velocity dispersions to behave as $1/t$ for long timescales.

To obtain the expression for the time evolution of the dispersions in configuration space we integrate the distribution function with respect to all velocities (see Eq. 2.6). In practice, we first transform $\sigma_\varpi(t)$ from polar to Cartesian coordinates, $\sigma'_\varpi(t) = (\mathbf{T}')^\dagger \sigma_\varpi(t) \mathbf{T}'$, where

$$
\mathbf{T}' = \begin{bmatrix}
-\dfrac{\sin(\psi)}{r} & \dfrac{\cos(\psi)}{r} & 0 & 0 \\
\dfrac{\cos(\psi)}{} & \sin(\psi) & 0 & 0 \\
\dfrac{\sin(\psi)p_r}{r} & -\dfrac{\cos(\psi)p_r}{r} & -\sin(\psi) & \cos(\psi) \\
-\dfrac{\sin(\psi)v_\psi}{r} & \dfrac{\cos(\psi)v_\psi}{r} & \cos(\psi) & \sin(\psi)
\end{bmatrix}. \tag{2.19}
$$

We express σ'_ϖ as

$$
\sigma'_\varpi = \begin{pmatrix} \mathbf{A} & \mathbf{B} \\ \mathbf{B}^\dagger & \mathbf{C} \end{pmatrix},
$$

where the 2x2 matrices $\mathbf{A}$, $\mathbf{C}$ and $\mathbf{B}$ represent the position submatrix, the velocity submatrix, and the cross correlation between positions and velocities, respectively (as in Eq. 2.3). Then, the matrix $\sigma_\mathbf{x}$ is obtained from the integration of the distribution function over the velocities:

$$
\sigma_\mathbf{x} = \begin{pmatrix} s_{11} & s_{12} \\ s_{12} & s_{22} \end{pmatrix},
$$

where the elements s_{ij} are related to the dispersions in configuration space. These elements can be expressed as:

$$
s_{ij} = \frac{\det \mathbf{\Gamma}_{ij}}{\det \mathbf{C}}, \tag{2.20}
$$

with

$$
\mathbf{\Gamma}_{ij} = \begin{pmatrix}
a_{ij} & b_{i1} & b_{i2} \\
b_{j1} & c_{11} & c_{12} \\
b_{j2} & c_{12} & c_{22}
\end{pmatrix},
$$

where a_{ij}, b_{ij} and c_{ij} are elements of the matrices $\mathbf{A}$, $\mathbf{B}$ and $\mathbf{C}$ respectively. The diagonalisation of the matrix $\sigma_\mathbf{x}$ yields the values of the dispersions along the principal axes of the system in configuration space since $\sigma_{x_i} = 1/\sqrt{\lambda_{r_i}}$, where λ_{r_i} are the eigenvalues of $\sigma_\mathbf{x}$.

Solving the characteristic equation for $\sigma_\mathbf{x}$ we finally obtain:

$$
\begin{aligned}
\lambda_{r_i} = {} & (2\lambda_{v_1}\lambda_{v_2})^{-1} \Big[\beta_2 t^2 + \beta_1 t + \beta_0 \pm \\
& \sqrt{(\beta_2 t^2 + \beta_1 t + \beta_0)^2 - 4\lambda_{v_1}\lambda_{v_2} \det \sigma_w^0} \Big],
\end{aligned} \tag{2.21}
$$

where

$$
\begin{aligned}
\beta_2 &= \sigma_{11}\sigma_{22}r^2\left[(\sigma_{44}\Omega'^2_{34} + \sigma_{33}\Omega'^2_{44})(p_r^2 + r^2\kappa^2) - \right. \tag{2.22}\\
&\quad \left. 2\Omega'_{34}(\sigma_{44}\Omega'_{33} + \sigma_{33}\Omega'_{44})r^2\kappa\Omega_r + (\sigma_{44}\Omega'^2_{33} + \sigma_{33}\Omega'^2_{34})r^2\Omega_r^2\right], \\
\beta_1 &= -2\sigma_{11}\sigma_{22}r^2\left[(\sigma_{44}W_{34}\Omega'_{34} + \sigma_{33}W_{44}\Omega'_{44})(p_r^2 + r^2\kappa^2) + \right. \\
&\quad \left((\sigma_{33}W_{44} + \sigma_{44}W_{33})\Omega'_{34} + W_{34}(\sigma_{44}\Omega'_{33} + \sigma_{33}\Omega'_{44})\right)r^2\kappa\Omega_r - \\
&\quad \left. (\sigma_{44}W_{33}\Omega'_{33} + \sigma_{33}W_{34}\Omega'_{34})r^2\Omega_r^2\right], \\
\beta_0 &= r^2\left[\sigma_{11}\left(\sigma_{22}\sigma_{33}W_{44}^2 + \sigma_{44}(\sigma_{22}W_{34}^2 + \sigma_{33})\right)(p_r^2 + r^2\kappa^2) - \right. \\
&\quad 2\sigma_{11}\sigma_{22}W_{34}(\sigma_{33}W_{44} + \sigma_{44}W_{33})r^2\kappa\Omega_r + \\
&\quad \left. \sigma_{22}\left(\sigma_{11}\sigma_{33}W_{34}^2 + \sigma_{44}(\sigma_{11}W_{33}^2 + \sigma_{33})\right)r^2\Omega_r^2\right]. \tag{2.23}
\end{aligned}
$$

Finally, multiplying both eigenvalues:

$$
\lambda_{r_1}\lambda_{r_2} = \frac{\det\sigma_w^0}{\lambda_{v_1}\lambda_{v_2}}. \tag{2.24}
$$

Bibliography

Arad I., Lynden-Bell D., 2005, MNRAS, 361, 385

Athanassoula E., Fady E., Lambert J. C., Bosma A., 2000, MNRAS, 314, 475

Binney J., 2004, MNRAS, 350, 939

Binney J., Tremaine S., 2008, Galactic Dynamics: Second Edition, ed. J. Binney & S. Tremaine (Princeton University Press)

Dehnen W., 2001, MNRAS, 324, 273

Diemand J., Moore B., Stadel J., Kazantzidis S., 2004, MNRAS, 348, 977

El-Zant A. A., 2002, MNRAS, 331, 23

Gerhard O. E., Saha P., 1991, MNRAS, 251, 449

Goldstein H., 1959, Classical Mechanics, ed. H. Goldstein (Addison-Wesley)

Goodman J., Heggie D. C., Hut P., 1993, ApJ, 415, 715

Hayes W. B., 2003, ApJ, 587, L59

Helmi A., White S. D. M., 1999, MNRAS, 307, 495

Hemsendorf M., Merritt D., 2002, ApJ, 580, 606

Hut P., Heggie D. C., 2001, ArXiv Astrophysics e-prints

Kandrup H. E., 1998, MNRAS, 301, 960

Kandrup H. E., Mahon M. E., 1994, A&A, 290, 762

Kandrup H E., Sideris I. V., 2001, Phys. Rev. E, 64, 056209

Kandrup H. E., Sideris I. V., 2003, ApJ, 585, 244

Kandrup H. E., Smith H. J., 1991, ApJ, 374, 255

Lecar M., 1968, Bull. Astron., 3, 91

Lichtenberg A. J., Lieberman M. A., 1983, Regular and stochastic motion, ed. A. J. Lichtenberg & M. A. Lieberman

Lynden-Bell D., 1967, MNRAS, 136, 101

McGill C., Binney J., 1990, MNRAS, 244, 634

Merritt D., 1996, AJ, 111, 2462

Miller R. H., 1964, ApJ, 140, 250

Quinlan G. D., Tremaine S., 1992, MNRAS, 259, 505

Sideris I. V., 2004, Celestial Mechanics and Dynamical Astronomy, 90, 147

Springel V., Yoshida N., White S. D. M., 2001, New Astronomy, 6, 79

Valluri M., Merritt D., 2000, in The Chaotic Universe, Proceedings of the Second ICRA Network Workshop, Advanced Series in Astrophysics and Cosmology, vol.10, World Scientific, ed. V. G. Gurzadyan & R. Ruffini, 229

Valluri M., Vass I. M., Kazantzidis S., Kravtsov A. V., Bohn C. L., 2007, ApJ, 658, 731

Vass I. M., Kazantzidis S., Valluri M., Kravtsov A. V., 2009, ApJ, 698, 1813

Vogelsberger M., White S. D. M., Helmi A., Springel V., 2008, MNRAS, 385, 236